



ORIGINAL ARTICLE

Assessment of image features for vessel wall segmentation in intravascular ultrasound images

Lucas Lo Vercio^{1,2} · José Ignacio Orlando^{1,2} · Mariana del Fresno^{1,3} · Ignacio Larrabide^{1,2}

Received: 13 January 2015 / Accepted: 24 December 2015 / Published online: 25 January 2016
© CARS 2016

Abstract

Background Intravascular ultrasound (IVUS) provides axial greyscale images, allowing the assessment of the vessel wall and the surrounding tissues. Several studies have described automatic segmentation of the luminal boundary and the media–adventitia interface by means of different image features.

Purpose The aim of the present study is to evaluate the capability of some of the most relevant state-of-the-art image features for segmenting IVUS images. The study is focused on Volcano 20 MHz frames not containing plaque or containing fibrotic plaques, and, in principle, it could not be applied to frames containing shadows, calcified plaques, bifurcations and side vessels.

Methods Several image filters, textural descriptors, edge detectors, noise and spatial measures were taken into account. The assessment is based on classification techniques previously used for IVUS segmentation, assigning to each pixel a continuous likelihood value obtained using support vector machines (SVMs). To retrieve relevant features, sequential feature selection was performed guided by the area under the precision–recall curve (AUC-PR).

Results Subsets of relevant image features for lumen, plaque and surrounding tissues characterization were obtained, and SVMs trained with these features were able to accurately identify those regions. The experimental results were evaluated with respect to ground truth segmentations from a

publicly available dataset, reaching values of AUC-PR up to 0.97 and Jaccard index close to 0.85.

Conclusion Noise-reduction filters and Haralick's textural features denoted their relevance to identify lumen and background. Laws' textural features, local binary patterns, Gabor filters and edge detectors had less relevance in the selection process.

Keywords IVUS · Vessel wall · Segmentation · Feature selection · SVM

Introduction

Cardiovascular disease is one of the leading causes of hospitalization and death in the Occidental world. The atherosclerotic plaque interferes with the flow of blood modifying the mechanical characteristics of the vessel wall, inducing positive remodelling, and increasing the risk of thrombi or intimal hyperplasia [11]. Since angiography images capture only the lumen of the vessel, intravascular ultrasound (IVUS) has emerged as a valuable support study. IVUS is an imaging technique based on the combination of a catheter and an ultrasound transducer which captures axial images, in a way that allows the visualization of the vessel wall tissue and plaque composition. A variety of transducer technologies can be found, resulting in studies with different spatial resolution [22]. Typically, the frame rate is 25–30 fps and the catheter is pulled back at 0.5–1 mm/s, providing a large amount of information.

Considering the large number of images resulting from an IVUS study, automatic segmentation of the vessel wall is relevant to support diagnosis and interventional procedures. State-of-the-art methods can be classified into two main categories, being based on either image series [15, 20, 26] or a single slide [17, 29, 30]. Both fully and semi-automatic

✉ Lucas Lo Vercio
lucaslovercio@conicet.gov.ar

¹ Pladema, UNICEN, Tandil, Argentina

² CONICET, Tandil, Argentina

³ CIC-PBA, Tandil, Argentina

strategies can be found in each of these groups. Developing methods for vessel wall segmentation and plaque assessment in IVUS images is challenging due to the presence of speckle noise, artefacts and different imaging characteristics such as the variety of resolutions. Each of the existing solutions focuses on specific image features to capture appropriate information, and some of them are recurrently considered by different authors [16]. Noise-reduction filters such as nonlinear filtering [26, 30] and anisotropic diffusion [12, 17] were previously applied to IVUS images for lumen–intima and media–adventitia segmentation. Textural analysis is frequently used for plaque characterization [6, 11] and also to differentiate arterial tissues [20, 25].

The aim of this paper is to assess the efficiency of different state-of-the-art image features for lumen, plaque and surrounding tissues characterization. The segmentation technique used for guiding the feature selection process is not novel, and it is inspired by [12, 20, 25]. The study was focused on 20MHz Volcano frames that do not contain plaque or that contain fibrotic plaques. In principle, the conclusions achieved in this work could not be extrapolated directly to frames containing shadows, calcified plaques, bifurcations and/or side vessels. However, the feature selection process we used here is general enough to be applied in other kind of images. This processing step might be used, in part or as a whole, to finally segment the lumen–intima and media–adventitia interfaces. During the feature selection processes, the support vector machine (SVM) method was used to assign the pixels likelihood of belonging to an arterial region, and the precision–recall curve was generated to evaluate the capability of a feature set to discriminate arterial regions.

The remainder of this paper is organized as follows. Section 2 describes the dataset of IVUS images used in the experiments. Section 3 summarizes the strategy for feature extraction and selection, and the classifier we used. Section 4 presents our results, while Sect. 5 includes a discussion on them. Finally, Sect. 6 concludes the paper.

Materials

Our experiments were carried out using the publicly available dataset of IVUS images provided in [4]. This dataset comprises 435 images, 384×384 sized, acquired using Si5 imaging system (Volcano Corporation, California, USA) equipped with a 20MHz Eagle Eye catheter (Fig. 1a). Manual annotations of the luminal boundary and the media–adventitia interface are available for each image. In this study, a subset S of 149 images, without artefacts, shadows, bifurcations or side vessels, was selected. For the proper assessment of the learning algorithm, the set S was separated into a training–validation set, containing 107 images from seven studies, and a test set, containing 42 images from three stud-

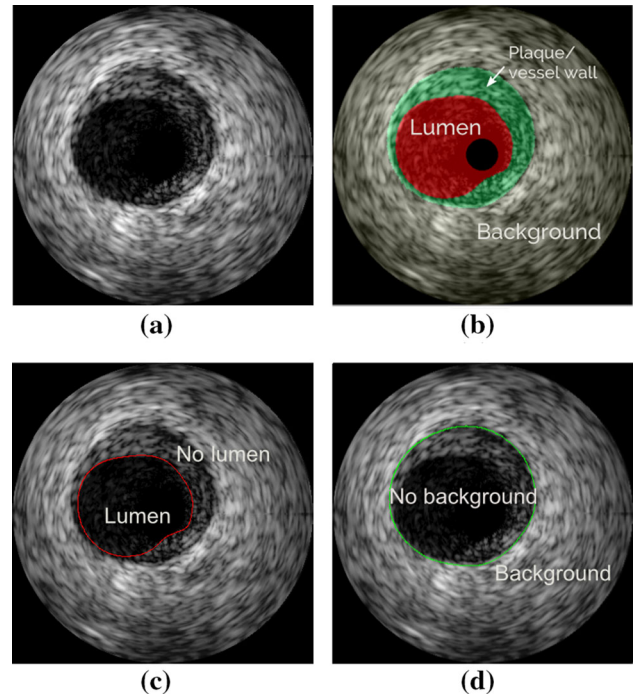


Fig. 1 **a** Original IVUS image. **b** Regions of interest: lumen, plaque/vessel wall and *Background*. **c** *Lumen/no lumen* classes. **d** *Background/no background* classes

ies. For the model adjustment step, the training–validation set was split using fivefold cross-validation to prevent overfitting [14]. Each pixel of the image was labelled using the annotations of the luminal boundary or lumen–intima (LI) and media–adventitia (MA) interfaces. The pixels within LI were labelled as *Lumen*, and the pixels outside MA were labelled as *Background*.

Methods

The problem of identifying the arterial wall was modelled as two different characterization problems (Fig. 1b). First, different features were evaluated to distinguish between *lumen/no lumen*, so that the lumen–intima interface (Fig. 1c) can be estimated as the border between those two regions. A separate feature set was retrieved to distinguish between *background/no background*, so the media–adventitia interface (Fig. 1d) can be similarly assessed by taking the frontier between these other regions.

Preprocessing

IVUS images were transformed to polar coordinates since it is useful to eliminate the empty regions corresponding to the corners and the catheter area, which also facilitates arterial tissues segmentation, due to their concentric disposition [29,

[30]. As the number of transducers in IVUS systems is usually a power of two, the sampling was performed using an angle increment of 0.703° , to obtain a lateral resolution of 512. The radial sampling step was 1 pixel, resulting in 512×173 sized polar images.

Image features

Several approaches were proposed in the literature for feature extraction in IVUS images, depending on the region of interest to be segmented or characterized. Two main groups of features were recognized: image filters, which homogenize and/or enhance certain regions and edges; and textural features, which characterize information of the heterogeneity of the image. The features described in this Section are summarized in Table 2.

Noise-reduction and edge-enhancement filters

IVUS images are affected by speckle noise, which is characteristic of ultrasound images [19]. Therefore, several noise-reduction filters were considered in this work. The image is convolved 25 times using a gaussian filter with $\sigma = 0.5$. The median filter was applied 25 times using 7×7 windows. This size was selected due to its good behaviour for window-based filters [19, 33]. The anisotropic diffusion [24] was performed 6000 times with two different values of the diffusion constant K : $K = 0.013$ homogenizes lumen preserving LI, but it does not reduce noise in plaque or *Background*; and $K = 0.023$, which homogenizes plaque and *Background*, preserves MA but smooths LI [19].

A number of specialized filters for speckle noise reduction have been recently proposed. The detail-preserving anisotropic diffusion (DPAD) [1] is a despeckling filter based on the Speckle Reducing Anisotropic Diffusion (SRAD) [33], which incorporates a model of the noise within the anisotropic diffusion. For the estimation of the coefficient of noise variation (C_u), the mode of local coefficients of variation C was applied on 5×5 windows, as the authors recommend. The step size was set to 0.2 and the filter was applied 1000 times since those parameters showed good homogenization of the lumen, the plaque and the *Background*.

The maximum averaged intensity is a filter specially designed for segmenting IVUS images, defined by

$$I_{\text{modified}}(x, y) = \max_{i \in [0, y]} \frac{1}{y - i + 1} \sum_{k=i}^y I(x, k), \quad (1)$$

where I is the image in polar coordinates. This filter smooths the lumen, and, at the same time, it enhances the lumen boundary [30].

Table 1 One-dimensional convolution kernels used for the computation of Law's textural features (Level 5)

Name	Kernel
Edge (E5)	(−1, −2, 0, 2, 1)
Spots (S5)	(−1, 0, 2, 0, −1)
Waves (W5)	(−1, 2, 0, −2, 1)
Ripples (R5)	(1, −4, 6, −4, 1)
Levels (L5)	(1, 4, 6, 4, 1)

Textural features

Haralick's textural descriptors [13, 28] are based on grey-level co-occurrence matrices (GLCMs), and they have been previously applied for IVUS segmentation [25] and plaque classification [6, 11]. The co-occurrences of the intensities in the images were extracted from 15×15 windows with two different configurations of distance (d) and orientation angles between pixels: N–S–E–W with $d = 1$ and N–S with $d = 1$ and $d = 2$. Image intensities were downsampled to 50 grey levels before computing the GLCMs, to reduce the computational cost. The calculated measures are the angular second moment, contrast, variance, inverse difference moment and entropy [13].

Laws' textural features are based on convolving the image with 5×5 kernels. These matrices are obtained by taking the outer product of all the possible combinations of five predefined one-dimensional convolution kernels (Table 1). After convolving the image with each matrix, 25 measures of texture energy were obtained by assigning to each pixel the sum of the absolute values in a 5×5 window [20].

Local binary patterns (LBP) are used to detect texture patterns in a circular neighbourhood. The LBP rotational invariant (LBP^{ri}) [23] was used with $R = [1, 2, 3]$ and the corresponding neighbourhood of $P = [8, 16, 24]$ [6].

2D Gabor filters are useful not only for detecting directional borders but also for texture analysis [5]. 16 Gabor kernels were considered, varying the standard deviation σ and the 2D frequencies (Φ, F): $\sigma_x = \sigma_y = [12.7205, 6.3602, 3.1801, 1.5901]$, with $\Phi = [0^\circ, 45^\circ, 90^\circ, 135^\circ]$, and the corresponding $F = [0.0442, 0.0884, 0.1768, 0.3536]$ [6]. The IVUS polar images were downsampled to a resolution of 256×256 pixels before computing the LBP and the Gabor features. We follow this approach to reproduce the feature extraction as it was performed in [7]. The resulting feature map was afterwards resized to the original image resolution.

The speckle index is a widely used estimator of the amount of speckle noise in laser and acoustic imaging [9, 33]. It was computed on the uncompressed B-mode image, following $q = \frac{\sigma}{\mu}$, where the mean μ and the standard deviation σ were calculated over 15×15 windows.

Spatial feature

The distance from the catheter was also included as a feature since it is a common reference for segmentation [29,34]. As the regions lumen, vessel wall/plaque and *background* are concentrically disposed, this feature reflects this spatial characteristic.

Shadow indicators

Two measures related to the cumulative grey level were taken into account, namely shadow (S_h) and relative shadow (S_r), defined by

$$S_h(x, y) = \frac{1}{N_r N_c} \sum_{y_s=y}^{N_r} BI(x, y_s) \quad (2)$$

and

$$S_r(x, y) = \frac{1}{N_r N_c} \sum_{y_s=y}^{N_r} y_s BI(x, y_s) \quad (3)$$

where BI is a binary image thresholding I with a threshold $TH = 14$, and N_r and N_c are the height and the width of the polar image, respectively [8].

Edge detection filters

The 3×3 Sobel, Laplacian and Prewitt kernels were applied. Although the aim of the present work is the assessment of features for region discrimination and not the borders among them, these edge indicators were also evaluated [8,12,26,29].

Feature selection

Time-complexity and memory requirements of a segmentation algorithm are highly dependant on the features that it uses. Thus, a minimal subset of relevant features is valuable. The aim of the feature selection process is to build such subset of features F_r , from the set of all available features F . Nevertheless, finding F_r is NP-hard.

Sequential forward selection is a greedy approach that allows to obtain a sub-optimal subset of features in polynomial time. This algorithm starts with an empty set of features F_r , and it iteratively incorporates new features only if they improve the results with respect to the previous configuration of F_r . Though the process should stop when adding more features does not improve the accuracy, we decided to force it to continue so it is possible to assess a larger number of features (Algorithm 1). One feature selection process was performed for each combination of training-validation within the K-fold. The results show that the accuracy mea-

sures do not improve after $|F_r| = 10$, though we continue the feature selection process until $|F_r| = 20$.

Algorithm 1 Sequential forward selection

```

 $F_r \leftarrow \emptyset$ 
 $\lambda s \leftarrow \{10^m, m = \{-7, \dots, -1\}\}$ 
for  $|F_r| \leftarrow 1 \dots 20$  do
     $p \leftarrow 0$ 
     $f_{best} \leftarrow \emptyset$ 
    for  $i \leftarrow 1 \dots |F|$  do
         $Q \leftarrow F_r \cup f_i$ 
        for  $j = 1 \dots |\lambda s|$  do
            Train SVM with  $Q$  and  $\lambda_j$ 
            Calculate AUC-PR  $\forall I$  of the validation set
            Calculate  $\mu$ (AUC-PR)
            if  $\mu$ (AUC-PR) >  $p$  then
                 $p \leftarrow \mu$ (AUC-PR)
                 $f_{best} \leftarrow f_i$ 
            end if
        end for
    end for
     $F_r \leftarrow F_r \cup f_{best}$ 
     $F \leftarrow F - f_{best}$ 
end for

```

Support vector machine

Support vector machines (SVMs) are supervised learning models that are widely used in several applications, including data mining and image segmentation [10,14,20]. SVMs are binary classifiers that are able to learn the optimal hyperplane that better separates two distributions of feature vectors in the feature hyperspace, according to a collection of training data. In this work, we applied SVM to characterize image pixels in the *lumen/no lumen* and *background/no background* categories separately.

Let the training set S be composed by N training samples (x_i, y_i) , where $x_i \in \mathbb{R}^M$ is the feature vector of a given pixel i , and $y_i \in \{-1, +1\}$ its corresponding true label (+1 is assigned to the class of interest and -1 to any other class). The set of all the feature vectors in S comprises a distribution in a M -dimensional feature space. In the ideal case, the distributions corresponding to both classes should be linearly separable by a hyperplane $\{\beta, \beta_0\}$, verifying:

$$y_i(\mathbf{x}_i^T \boldsymbol{\beta} + \beta_0) > 0. \quad (4)$$

The distance between the separating hyperplane and the closest points is called the *margin*. The SVM method manages to find the hyperplane $\{\beta, \beta_0\}$ that maximizes that margin.

By rescaling $\boldsymbol{\beta}$ and β_0 , Eq. 4 can be rewritten as

$$y_i(\mathbf{x}_i^T \boldsymbol{\beta} + \beta_0) > 1. \quad (5)$$

Thus, the margin is $1/\|\boldsymbol{\beta}\|$, and the maximization of the margin is equivalent to the minimization of $\|\boldsymbol{\beta}\|$.

In practice, the distributions of feature vectors are not usually linearly separable, but overlapped. In that case, the SVM minimization problem must be refined so vectors overpassing the hyperplane are allowed. This setting is provided by the introduction of the slack variables ξ_i , resulting in a soft margin of separation. The corresponding objective function to be minimized is given by the expression:

$$\min_{\beta, \beta_0} \frac{\lambda}{2} \|\beta\|^2 + \sum_{i=1}^N \xi_i^2 \quad (6)$$

subject to $y_i \mathbf{x}_i^T \beta + \beta_0 \geq 1 - \xi_i, \forall i$.

The regularization parameter $\lambda > 0$ is user-defined, as it controls the penalty of allowing the maximization of the margin or the minimization of the classification errors on the training set. In each step of the sequential forward selection, the value of λ is linearly adjusted by considering $\lambda \in 10^i$, with $i \in -7, -6, \dots, -1$. The one that maximizes the performance on the validation set is selected.

The predicted class of a new pixel t on the test set, with feature vector \mathbf{x}_t , is given by the sign of $f(\mathbf{x}_t) = \mathbf{x}_t^T \beta + \beta_0$.

The computational cost of solving the objective function (Eq. 6) is proportional to the number of pixels N on the training data. Due to the large size of the training sets ($N > 7 \times 10^6$ pixels), we approximate the solution by means of a linear SVM solver for large dataset, named Stochastic Dual Coordinate Ascent (SDCA) [27], as provided by [31].

Evaluation metrics

The proportion of *lumen/no lumen* in the IVUS images is 11–89 % when cartesian coordinates are considered, and 24–76 % when the images are transformed to polar coordinates. For *background/no background*, the proportions are 19–81 % and 36–64 %, respectively. This analysis shows a slight skewed-class problem even when using polar coordinates. As a consequence, the area under the precision–recall curve (AUC-PR) was chosen as accuracy measure since it better deals with label distribution problems than the typically area under the ROC curve [18]. The likelihood $f(\mathbf{x})$ was used to construct the PR curve. The higher the AUC-PR is, the more accurate the pixel classification will be. The PR curve implementation provided by Vedaldi and Fulkerson [31] was used.

The F1-score is a measure used for evaluating binary classifications with unbalanced classes. It is defined as the harmonic mean of precision and recall,

$$\text{F1-score} = 2 \times \frac{\text{precision} \cdot \text{recall}}{\text{precision} + \text{recall}}. \quad (7)$$

This metric was obtained by evaluating the binary segmentations obtained using the $\text{sign}(f(\mathbf{x}))$ rule.

Finally, for comparison with the results obtained on the IVUS segmentation challenge [4], Jaccard Measure (or Jaccard Index—JM) and Percentage of Area Difference (PAD) were calculated, previously transforming the resulting score maps to the cartesian domain. In this process, it is important restoring the blank area corresponding to the catheter, which was discarded when the image was transformed to polar coordinates.

Results

Figure 2a shows the first and last selection of each feature for the five training–validation folds performed for *lumen/no lumen* characterization. The horizontal shades highlight the feature groups described in Table 2, named image filters, spatial feature, noise feature, Haralick’s textural features, Laws’ textural features, local binary patterns, Gabor filters, shadow indicators and edge detectors. Similarly, Fig. 2b shows the feature selection for *background/no background* characterization.

Figure 3a depicts the evolution of AUC-PR and F1-score in the *lumen/no lumen* characterization on each training–validation fold and on the test set. At the moment of evaluating on the test set, the most frequent selected feature at each position of the fivefold was added to the feature set. The SVM was trained with the whole training–validation dataset using $\lambda = 0.0001$, which is the most frequently selected value when the measures reach stability. Similarly, Fig. 3b shows AUC-PR and F1-score in the *background/no background* characterization using the same criteria when evaluating on the test set.

Table 3 depicts the mean training time of an SVM as F_r grows. The experiments were conducted on an Intel i7-3630QM platform at 2.4 GHz, with 6 GB of RAM.

Table 4 shows the values of JM and PAD for the best subsets of features F_r found: $F_r = \{\mathbf{F1}, \mathbf{F6}, \mathbf{F10}\}$ for *lumen/no lumen* and $F_r = \{\mathbf{F1}, \mathbf{F3}, \mathbf{F6}, \mathbf{F8}, \mathbf{F18}, \mathbf{F64}\}$ for *background/no background* characterization.

Figure 4 shows an example of the pixel prediction on two polar IVUS images. These images were retrieved from the test set and they have been characterized using the best F_r for each problem. Figure 4a shows a vessel wall eccentric from the catheter position. Figure 4d corresponds to an image with a large plaque region.

Discussion

Lumen/no lumen characterization

Figure 2a, b shows that the intensity feature maximum intensity average (**F6**) is the one that was mostly chosen at

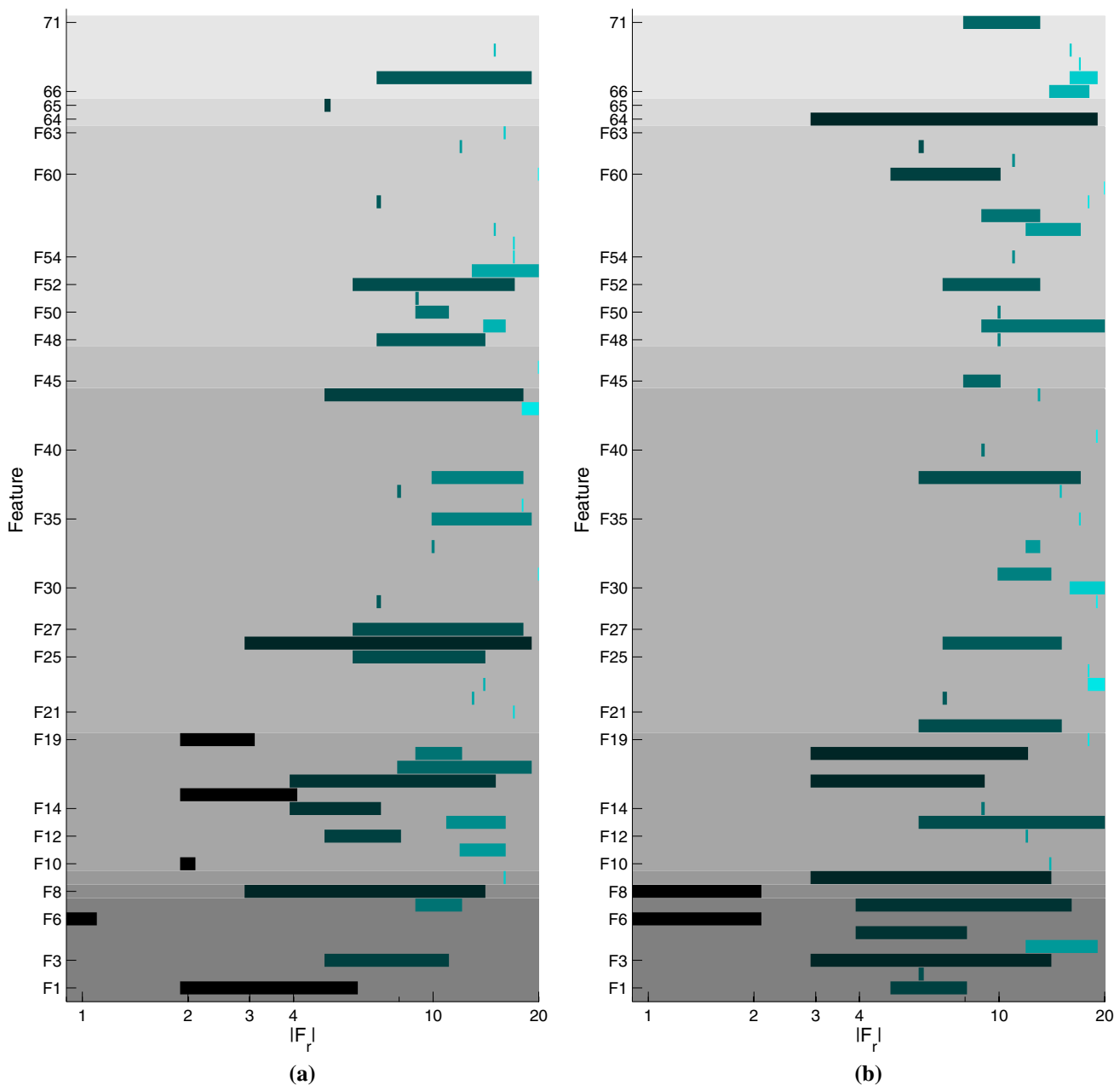


Fig. 2 Earlier and latest selection of each image feature (Table 2) during the feature selection for each fold. **a** Feature selection for *lumen/no lumen* characterization. **b** Feature selection for *background/no background* characterization

the first iteration of the feature selection processes. This behaviour can be explained by the high linear correlation between the feature value and the class labelling (-0.83 for *lumen/no lumen* and -0.81 for *background/no background*). For *lumen/no lumen*, the likelihood obtained using **F6** reached the AUC-PR up to 0.98 and F1-score was close to 0.92 (Fig. 3a), verifying the results of [30]. On the second and third iterations, the original image (**F1**) or Haralick's textural features were mostly selected (**F10**, **F15**, **F19**) over distance

from catheter (**F8**) and E5E5 (**F26**). AUC-PR had a slightly improvement to 0.988, and the F1-score reached 0.93. On the following iterations, no improvement is observed (Fig. 3a) and no group or feature was clearly selected (Fig. 2a). When $F_r = \{F1, F6, F10\}$, JM and PAD reached 0.83 and 0.18, respectively (Table 4). Figure 4b, e shows examples of *lumen/no lumen* characterization with a few noisy likelihoods in some pixels.

Table 2 Group, name and summarized description for each feature

Feature group	Name of feature	Summary
Image filters [19]	F1. Original polar image F2. Gaussian filter F3. Median filter F4–5. Perona–Malik F6. Maximum intensity average F7. Detail-preserving anisotropic diffusion	— Gaussian filter applied 25 times using $\sigma = 0.5$ Median filter applied 25 times using a 7×7 window [26] Anisotropic diffusion [24] applied with 6000 iterations using $K = 0.013$ and $K = 0.023$ Used in [30] Proposed by Aja-Fernández and Alberola-López [1]
Spatial feature	F8. Distance from catheter	Spatial feature
Noise feature [9]	F9. Speckle index	Calculated over a 15×15 window in the uncompressed B-mode image
Haralick's textural features [13,28]	F10. Angular second moment F11. Contrast F12. Sum of squares or Variance F13. Inverse difference moment F14. Entropy F15. Angular second moment F16. Contrast F17. Sum of squares or Variance F18. Inverse difference moment F19. Entropy	Calculated over a 15×15 window (N–S–E–W directions) Calculated over a 15×15 window (N–S directions)
Law's textural features [20]	F20–44. L5L5, L5E5, L5S5, L5W5, L5R5, E5L5, E5E5, E5S5, E5W5, E5R5, S5L5, S5E5, S5S5, S5W5, S5R5, W5L5, W5E5, W5S5, W5W5, W5R5, R5L5, R5E5, R5S5, R5W5, R5R5	5×5 convolving kernels. Each pixel is characterized with the energy of each textural feature
Local binary patterns (LBP)	F45–47 ($R = 1, P = 8$), ($R = 2, P = 16$), ($R = 3, P = 24$)	Used in [6]
Gabor filters	F48–63 (σ_x, ϕ, F) = [(12.7205, 0°, 0.0442), (6.3602, 0°, 0.0442), (3.1801, 0°, 0.0442), (1.5901, 0°, 0.0442), (12.7205, 45°, 0.0884), (6.3602, 45°, 0.0884), (3.1801, 45°, 0.0884), (1.5901, 45°, 0.0884), (12.7205, 90°, 0.1768), (6.3602, 90°, 0.1768), (3.1801, 90°, 0.1768), (1.5901, 90°, 0.1768), (12.7205, 135°, 0.3536), (6.3602, 135°, 0.3536), (3.1801, 135°, 0.3536), (1.5901, 135°, 0.3536)]	Used in [7]
Shadow indicators	F64. Shadow F65. Relative Shadow	Proposed by [8]
Edge detectors	F66–67. Sobel N–S and E–W direction F68–69. Prewitt N–S and E–W direction F70–71. Laplacian N–S and E–W direction	3×3 kernels. Basis of the canny edge detectors used in [8, 12, 26, 29]

Background/no background characterization

On the first iteration, by selecting **F6**, the AUC-PR was near 0.96 and F1-score is close to 0.88 (Fig. 3b). On the second iteration, distance from catheter (**F8**) was selected if

F6 was retrieved in the first iteration, or viceversa. This can be explained by the relatively low correlation (0.58) between these features, and **F8** is slightly inversely correlated (-0.77) with the *background/no background* labelling. This means that the new feature provided additional information.

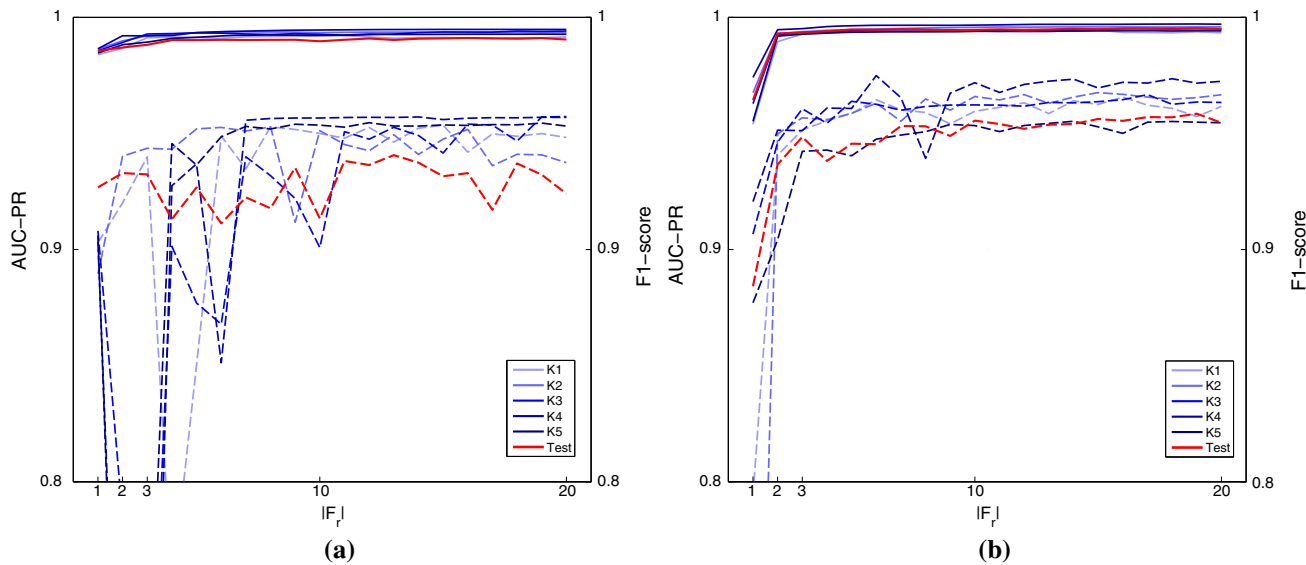


Fig. 3 Accuracy measures: AUC-PR (solid line) and F1-score (dashed line). Blue lines represent training-validation folds. Red lines represent measures on the test set. **a** Feature selection for *lumen/no lumen* characterization. **b** Feature selection for *background/no background* characterization

mation. AUC-PR went from 0.96 to 0.99, and F1-score had a remarkable growth from 0.88 to 0.93. On the third and fourth iterations, AUC-PR and F1-score slightly grew, adding to F_r an intensity feature (**F3**, **F5**, **F7**), Haralick's textural feature (**F16** and **F18**), the speckle index (**F9**) or the Shadow feature (**F64**). The linear correlations with the labelling have lower absolute value than features previously selected ($-0.71, -0.71, -0.73, -0.32, 0.33, -0.32$ and 0.5, respectively). However, in Fig. 3b, the slightly growth of the curves shows that they incorporated few additional information. The implications of the linear correlation between the features and classes and between features themselves in the feature selection process has been previously noticed in [32]. Beyond the fifth iteration, a more frequent feature in each iteration cannot be found, but still a feature can be added to F_r .

When $F_r = \{F1, F3, F6, F8, F18, F64\}$ JM and PAD attained 0.85 and 0.15, respectively (Table 4). Figure 4c, f shows a good separation between regions, although there are some values in the plaque region that can lead to misclassifications when segmenting.

General remarks

In Fig. 2a, b, a predominance of pure image intensity filters over other features can be observed, as they were selected earlier on the feature selection process. The early selection of **F3**, **F5** and **F7** verifies the good results of nonlinear filters previously stated in [19, 26]. The noisy original image (**F1**) was usually selected before the Gaussian filter **F2**. This is likely due to the fact that in **F1** the speckle noise remains

Table 3 SVM training time (in seconds)

	$ F_r $				
	1	3	6	10	20
Lumen/no lumen	1.27	1.68	2.00	2.50	4.59
Background/no background	1.36	1.56	2.02	2.59	4.43

Table 4 Mean(SD) values of Jaccard Measure (JM) and percentage of area difference (PAD) for the test set, using $F_r = \{F1, F6, F10\}$ for *lumen/no lumen* characterization, and $F_r = \{F1, F3, F6, F8, F18, F64\}$ for *background/no background* characterization. These measures are calculated in the cartesian coordinate system

	Lumen/no lumen	Background/no background
JM	0.83 (0.05)	0.85 (0.04)
PAD	0.18 (0.06)	0.15 (0.04)

punctual, but in **F2**, it propagates the noise to the neighbouring pixels.

Following image filters, Haralick's textural descriptors were selected over other features groups in both characterization problems. The capability of this textural feature family when segmenting IVUS has been previously noticed in [25]. Nevertheless, Laws' textural features are useful in [20] since they are used to adjust an initial contour inside a restricted neighbourhood of the image. It seems that LBP, Gabor filters and edge detectors will not be appropriate for segmenting the arterial wall under the conditions of the present work.

The distance from catheter (**F8**) is presented in fully automatic segmentation algorithms [12, 29, 30, 34], both in implicit or in explicit way. In our experiments, this feature

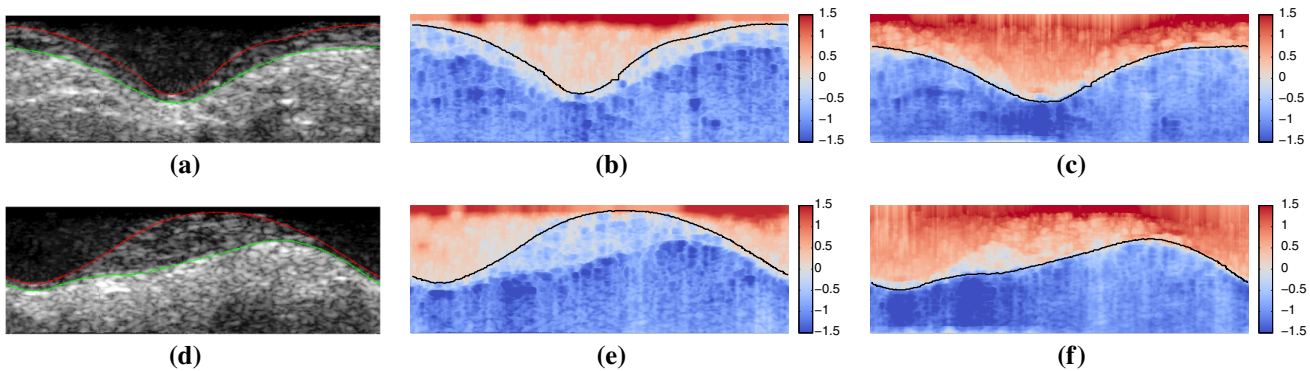


Fig. 4 Examples of the likelihoods obtained for each region of interest. Figures are marked with the reference segmentation and the likelihood (colour map proposed in [21]). **a, d** Lumen–intima marked in red, separating *lumen/no lumen*. Media–adventitia marked in green,

separating *background/no background*. **b, e** *Lumen/no lumen* characterization using $F_r = \{F1, F6, F10\}$. **c, f** *Background/no background* characterization using $F_r = \{F1, F3, F6, F8, F18, F64\}$

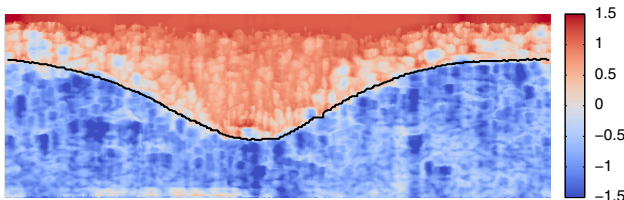


Fig. 5 Characterization of Fig. 4a for *background/no background* excluding **F8** from F_r ($F_r = \{F1, F3, F6, F18, F64\}$). The measures on the test set reached $AUC-PR=0.98(0.01)$, $PAD=0.2(0.05)$ and $JM=0.81(0.05)$

was always selected for *background/no background* characterization. Although this feature depends on the training data, Fig. 4c shows that the characterization generally performs well, even when the artery is eccentric from the catheter position. Analysing the weights of β , the distance from catheter affects the prediction $f(\mathbf{x})$ less than 25 %, in comparison with the remaining features in F_r . Figure 5 shows the impact of the absence of **F8** from the subset of relevant features.

Most of the participants in the IVUS segmentation challenge, presented at the CVII workshop at MICCAI 2011 conference [4], used the features analysed in the present work for their segmentation methods, such as [8, 20, 26, 30]. Images with artefacts, shadows, bifurcations or side vessels were excluded from ours experiments since each one of these characteristic should be processed in a different way than the arterial wall tissue [2, 29, 30]. The resulting values of JM and PAD, obtained with a simple thresholding, are close to the reported values of the challenge for images having only plaque (Table 4). These values demonstrate the feasibility of segmenting IVUS images using SVMs and the retrieved image features. The proposed characterization scheme can be integrated with a segmentation technique that exploits other

intrinsic characteristics to determine a unique contour of LI and MA.

The presence of irrelevant features in the feature space prevents the proper separation of points, for example, by a cutting plane. *A priori*, at later iterations of the feature selection, undesired features will diminish the accuracy. Nevertheless, SVM deals well with irrelevant features due to the value of the parameter λ and the addition of slack variables. Different values of λ were recurrently tested during the sequential feature selection. As the size of the selected feature set grew and less relevant features were added, higher values of λ were required to remain high the AUC-PR and F1-score values (Fig. 3). A similar behaviour of feature selection and SVMs was previously observed in [10]. Furthermore, our experimental results show that the training time of the SVM using 20 features takes 2 times more than using 6 features as we propose (Table 3).

Finally, the K-fold cross-validation successfully avoids overfitting. Figure 3 shows that the quality measures behave similarly when evaluated on the training and test sets, with slightly smaller values, as theoretically expected [3].

Conclusions

An analysis of image features for IVUS segmentation was presented. It was based on a sequential forward selection process using SVMs and the PR curve. Moreover, a successful dimensionality reduction of the image feature space was achieved, decreasing the computational resources for feature extraction and training.

Image filters, such as the maximum intensity average, the original image and the median filtered image, and Haralick's textural features, specially when characterizing N-S

direction, demonstrated better discrimination capability for arterial regions than other image features.

AUC-PR showed to be useful to guide the feature selection process. The resulting values of AUC-PR, F1-score, JM and PAD, for IVUS images not containing plaque or presenting a fibrotic one, indicate that segmentation of IVUS images using SVMs is feasible, but it can be improved since it still can lead to the presence of misclassifications and features such as calcified plaques, bifurcations and side vessels. Furthermore, the determination of an unique contour of LI or MA from the score map is not trivial, as the qualitative results exhibit.

Finally, the K-fold cross-validation with $K = 5$ prevented overfitting, and the strength of the SVM as classifier in presence of irrelevant features has been shown.

Acknowledgments The present work has been partially funded by the National Agency for Science and Technology Promotion (ANPCyT, Argentina) within the projects PICT 2010-1287 and PICT 2014-1730.

Compliance with ethical standards

Conflict of interest The authors have no conflicts of interest.

References

1. Aja-Fernández S, Alberola-López C (2006) On the estimation of the coefficient of variation for anisotropic diffusion speckle filtering. *IEEE Trans Image Process* 15(9):2694–2701
2. Alberti M, Balocco S, Gatta C, Ciompi F, Pujol O, Silva J, Carrillo X, Radeva P (2012) Automatic bifurcation detection in coronary IVUS sequences. *IEEE Trans Biomed Eng* 59(4):1022–1031
3. Alpaydin E (2010) Introduction to machine learning, 2nd edn. MIT Press, Cambridge
4. Balocco S, Gatta C, Ciompi F, Wahle A, Radeva P, Carlier S, Unal G, Sanidas E, Mauri J, Carrillo X, Kovarnik T, Wang CW, Chen HC, Exarchos TP, Fotiadis DI, Destrempe F, Cloutier G, Pujol O, Alberti M, Mendizabal-Ruiz EG, Rivera M, Aksoy T, Downe RW, Kakadiaris IA (2014) Standardized evaluation methodology and reference database for evaluating IVUS image segmentation. *Comput Med Imaging Graph* 38(2):70–90
5. Bovik A, Clark M, Geisler W (1990) Multichannel texture analysis using localized spatial filters. *Pattern Anal Mach Intell IEEE Trans* 12(1):55–73
6. Caballero K, Barajas J, Pujol O, Rodriguez O, Radeva P (2007) Using reconstructed IVUS images for coronary plaque classification. In: Engineering in Medicine and Biology Society, EMBS 2007. 29th annual international conference of the IEEE, pp 2167–2170
7. Ciompi F (2008) Ecoc-based plaque classification using in-vivo and ex-vivo intravascular ultrasound data. Master's thesis, CVC-UAB
8. Ciompi F, Pujol O, Gatta C, Alberti M, S B, Carrillo X, Mauri-Ferre J, Radeva P (2012) Holimab: a holistic approach for mediaadventitia border detection in intravascular ultrasound. *Med Image Anal* 16:1085–1100
9. Crimmins TR (1985) Geometric filter for speckle reduction. *Appl Opt* 24(10):1438–1443
10. Giannoglou V, Stavrakoudis D, Theocharis J (2012) IVUS-based characterization of atherosclerotic plaques using feature selection and svm classification. In: 2012 IEEE 12th international conference on bioinformatics bioengineering (BIBE), pp 715–720
11. Giannoglou VG, Stavrakoudis DG, Theocharis JB, Petridis V (2015) Genetic fuzzy rule based classification systems for coronary plaque characterization based on intravascular ultrasound images. *Eng Appl Artif Intell* 38:203–220
12. Gil D, Hernandez A, Rodriguez O, Mauri J, Radeva P (2006) Statistical strategy for anisotropic adventitia modelling in IVUS. *IEEE Trans Med Imaging* 25(6):768–778
13. Haralick R, Shanmugam K, Dinstein I (1973) Textural features for image classification. *Syst Man Cybern IEEE Trans SMC* 3(6):610–621
14. Hastie T, Tibshirani R, Friedman J (2009) The elements of statistical learning: data mining, inference, and prediction. Springer, Berlin
15. Jourdain M, Meunier J, Sequeira J, Cloutier G, Tardif JC (2010) Intravascular ultrasound image segmentation: a helical active contour method. In: Image processing theory tools and applications (IPTA), 2010 2nd international conference on, pp 92–97
16. Katouzian A, Angelini E, Carlier S, Suri J, Navab N, Laine A (2012) A state-of-the-art review on segmentation algorithms in intravascular ultrasound (IVUS) images. *IEEE Trans Inf Technol Biomed* 16(5):823–834
17. Koga T, Uchino E, Suetake N (2011) Automated boundary extraction and visualization system for coronary plaque in IVUS image by using fuzzy inference-based method. In: 2011 IEEE international conference on fuzzy systems (FUZZ), pp 1966–1973
18. Liu Y, Shriberg E (2007) Comparing evaluation metrics for sentence boundary detection. In: Acoustics, speech and signal processing, ICASSP 2007. IEEE international conference on, vol 4, pp IV-185–IV-188
19. Loizou C, Pattichis C (2008) Despeckle filtering algorithms and software for ultrasound imaging. Morgan and Claypool, San Rafael
20. Mendizabal-Ruiz EG, Rivera M, Kakadiaris IA (2013) Segmentation of the luminal border in intravascular ultrasound b-mode images using a probabilistic approach. *Med Image Anal* 17(6):649–670
21. Moreland K (2009) Diverging color maps for scientific visualization. In: Bebis G, Boyle R, Parvin B, Koracin D, Kuno Y, Wang J, Pajarola R, Lindstrom P, Hinkenjann A, Encarnao ML, Silva CT, Coming D (eds) Advances in visual computing. Lecture notes in computer science, vol 5876. Springer, Berlin, pp 92–103
22. Nissen SE, Yock P (2001) Intravascular ultrasound: novel pathophysiological insights and current clinical applications. *Circulation* 103(4):604–616
23. Ojala T, Pietikainen M, Maenpaa T (2002) Multiresolution gray-scale and rotation invariant texture classification with local binary patterns. *IEEE Trans Pattern Anal Mach Intell* 24(7):971–987
24. Perona P, Malik J (1990) Scale-space and edge detection using anisotropic diffusion. *IEEE Trans Pattern Anal Mach Intell* 12(7):629–639
25. Pujol O, Rosales M, Radeva P, Nofrarias-Fernández E (2003) Intravascular ultrasound images vessel characterization using adaboost. In: Magnin I, Montagnat J, Clarysse P, Nenonen J, Katila T (eds) Functional imaging and modeling of the heart. Lecture notes in computer science, vol 2674. Springer, Berlin, pp 242–251
26. Sanz-Requena R, Moratal D, García-Sánchez DR, Bodí V, Rieta JJ, Sanchis JM (2007) Automatic segmentation and 3D reconstruction of intravascular ultrasound images for a fast preliminary evaluation of vessel pathologies. *Comput Med Imaging Graph* 31(2):71–80
27. Shalev-Shwartz S, Zhang T (2013) Stochastic dual coordinate ascent methods for regularized loss. *J Mach Learn Res* 14(1):567–599
28. Shapiro R, Haralick R (1992) Computer and robot vision. Addison-Wesley, Boston
29. Taki A, Najafi Z, Roodaki A, Setarehdan S, Zoroofi R, Konig A, Navab N (2008) Automatic segmentation of calcified plaques and

- vessel borders in IVUS images. *Int J Comput Assist Radiol Surg* 3(3–4):347–354
- 30. Unal G, Bucher S, Carlier S, Slabaugh G, Fang T, Tanaka K (2008) Shape-driven segmentation of the arterial wall in intravascular ultrasound images. *IEEE Trans Inf Technol Biomed* 12(3):335–347
 - 31. Vedaldi A, Fulkerson B (2008) VLFeat: an open and portable library of computer vision algorithms. <http://www.vlfeat.org/>
 - 32. Yu L, Liu H (2004) Efficient feature selection via analysis of relevance and redundancy. *J Mach Learn Res* 5:1205–1224
 - 33. Yu Y, Acton S (2002) Speckle reducing anisotropic diffusion. *IEEE Trans Image Process* 11(11):1260–1270
 - 34. Zhu X, Zhang P, Shao J, Cheng Y, Zhang Y, Bai J (2011) A snake-based method for segmentation of intravascular ultrasound images and its in vivo validation. *Ultrasonics* 51(2):181–189